

pubs.acs.org/journal/ascecg Research Article

Synthesis of V₂O₅ Nanoribbon—Reduced Graphene Oxide Hybrids as Stable Aqueous Zinc-Ion Battery Cathodes via Divalent Transition Metal Cation-Mediated Coprecipitation

Kamalambika Muthukumar, Sabari Rajendran, Archana Sekar, Ya Chen, and Jun Li*



Cite This: ACS Sustainable Chem. Eng. 2023, 11, 2670–2679



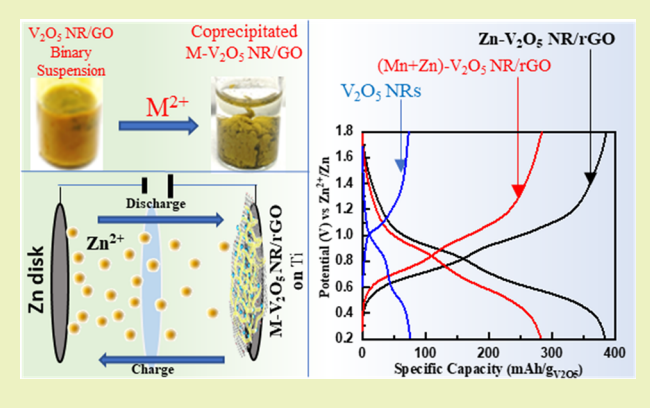
ACCESS I

III Metrics & More

Article Recommendations

s Supporting Information

ABSTRACT: Aqueous zinc-ion batteries (AZIBs) are an emerging sustainable and safer technology for large-scale electrical energy storage. Here, we report the synthesis of hybrid materials consisting of V_2O_5 nanoribbons (NRs) and reduced graphene oxide (rGO) nanosheets as AZIB cathode materials by divalent metal cation-mediated coprecipitation. The divalent metal ions M^{2+} (Zn²⁺ and Mn^{2+}) effectively neutralize the negative charges on the surface of microwave-exfoliated crystalline V_2O_5 NRs and graphene oxide (GO) nanosheets to form a strongly bound assembly. After thermal annealing in a nitrogen atmosphere, GO is converted into rGO with higher electrical conductivity while the layers in V_2O_5 NRs are expanded by M^{2+} intercalation. When only Zn²⁺ ions are used during coprecipitation, the produced Zn- V_2O_5 NR/rGO hybrid shows a very high reversible specific capacity of \sim 395 mAh g⁻¹ at 0.50 A g⁻¹ but



suffers from poor stability. This is improved by mixing Mn^{2+} with Zn^{2+} ions during coprecipitation. The (Mn + Zn)- V_2O_5 NR/rGO hybrid shows a slightly lower specific capacity of ~291 mAh g^{-1} at 0.5 A g^{-1} but a substantially improved long-cycling stability and better rate performance due to the stronger binding of Mn atoms in the V_2O_5 host that serve as stable pillars to support the expanded V_2O_5 layers.

KEYWORDS: hybrid electrode materials, microwave-assisted exfoliation, V_2O_5 nanoribbons, reduced graphene oxide nanosheets, aqueous zinc-ion batteries, divalent metal ion-mediated coprecipitation

INTRODUCTION

Aqueous zinc-ion batteries (AZIBs) have attracted extensive attention as potential sustainable electrical energy storage (EES) systems beyond Li-ion batteries (LIBs) due to Zn metal's high abundance and high specific volumetric capacity (5844 mAh cm⁻³).¹⁻³ In addition, Zn metal anodes have a higher redox potential (-0.76 V versus standard hydrogen electrode (SHE)) than other metal anodes, which makes them stable and usable in safer and more conductive aqueous electrolytes. 1-5 Particularly, AZIBs are an attractive nextgeneration sustainable technology for grid-scale EES. Despite the advantages, AZIBs face great challenges due to the large radius of the hydrated Zn²⁺ ions (5.5 Å),⁶ though the Shannon's ionic radius of Zn2+ is comparable to that of Li+ (0.74 Å versus 0.76 Å). The high electrostatic interaction due to Zn2+ ions' divalent cationic nature also causes large structural disruption to the host cathode materials, leading to low Coulombic efficiency (CE) and low electrode stability. One of the top priorities in AZIB research is to develop suitable cathode materials that exhibit reversible Zn²⁺ ion intercalation/deintercalation with acceptable energy density and stability. In the past, transition metal oxides and sulfides (such as V_2O_5 , MnO_2 , MoS_2 , VS_2 , etc.), $^{7-10}$ Prussian blue analogues, 11 and other inorganic materials 12,13 have been studied. Since the cell voltage of AZIBs (<1.8 V) is much lower than that of LIBs (\sim 3.5 V), a stable cathode close to their theoretical specific capacity is particularly important to enable practical AZIBs. 3,4

Among the transition metal oxides, the layered orthorhombic $\alpha\text{-}V_2O_5$ is particularly attractive due to its low cost, high theoretical specific gravimetric capacity (294 mAh g $^{-1}$ for 1 Zn^{2+} per V_2O_5), layered structure, and tunable oxidation states (as V $^{5+}$, V $^{4+}$, and V $^{3+}$). But, pure-phase bulk V_2O_5 suffers from low Zn $^{2+}$ ion diffusion coefficient, poor electronic conductivity, and structural instability. Nanostructured V_2O_5 has been explored to make use of its high specific

Received: December 24, 2022 Revised: January 18, 2023 Published: January 30, 2023





surface area (SSA), larger electrode-electrolyte interface, and shorter Zn²⁺ ion diffusion distance. Conductive carbon materials (such as graphene) have been incorporated with nanostructured V_2O_5 as stable structural supports and efficient electronic pathways. 15-17 Studies reported high specific capacities exceeding the 294 mAh g⁻¹ theoretical value (some even over 400 mAh g⁻¹) but suffered from poor cycling stability and possible water co-insertion.³ Another approach is to expand the spacing between the V2O5 layers by inserting water or metal cations.³ Nazar et al.¹⁸ reported a fast microwave-assisted synthesis of hydrated V₂O₅ nanobelts with the elemental formula of $Zn_{0.25}V_2O_5 \cdot nH_2O$. The Zn^{2+} cations were pre-intercalated between the V2O5 layers to serve as structural pillars that hold the expanded layers together before being used as AZIB cathodes. This was found to effectively improve the structural stability, yielding a relatively high specific capacity of 260 mAh $\rm g^{-1}$ at 2400 mA $\rm g^{-1}$ charge– discharge rate and an exceptional capacity retention of over 80% after 1000 cycles. Pre-intercalation of Na⁺ cations in the V₂O₅ nanowires with a formula of Na_{0,33}V₂O₅ was also found to stabilize the expanded layer structure and provided a high specific capacity of 360.7 mAh g⁻¹ with good stability. ¹⁹ Other metal-cation-inserted V_2O_5 materials, such as $Ca_{0.25}V_2O_5$: $nH_2O_7^{20}$ $K_{0.25}V_2O_5$, and $Mg_xV_2O_5$: $nH_2O_7^{22}$ were also reported to enhance the long-cycling stability in AZIBs. However, such layer-expanded materials in general suffer from poor electronic conductivity, which can be improved by incorporating conductive carbon-based templates.²

Inspired by the aforementioned studies, we have previously developed a liquid-phase exfoliation technique using a microwave-assisted process, 24 which produces $\rm V_2O_5$ nanoribbons (NRs) at a high yield (~20%) in 40 min, about 12 times faster than conventional hydrothermal methods. The $\rm V_2O_5$ NRs were further assembled with graphene oxide (GO) nanosheets by neutralizing the negative charges on the surface of both materials using Na $^+$ cations in a Na $_2\rm SO_4$ solution, forming an intimate $\rm V_2O_5$ NR/GO hybrid. GO was then converted into more conductive reduced graphene oxide (rGO) by thermal annealing in a N $_2$ atmosphere. The thus-prepared $\rm V_2O_5$ NR/rGO hybrid material showed a high performance as electrochemical supercapacitors. 24

Here, we extend this method using divalent transition metal cations M²⁺ (such as Zn²⁺ or Mn²⁺) from a solution of thermal decomposable acetate salts²⁵ to bind the 2D GO nanosheets (as the structural support) with the long 1D V_2O_5 NRs (as the active host materials) and study the hybrid materials as the AZIB cathodes in comparison to that of using monovalent Na⁺ ions. The microwave-exfoliated V₂O₅ NR is found to be a single-crystalline orthorhombic α-V₂O₅ material with welldefined crystal orientations. Its surface possesses a high negative charge density. The divalent metal ions M²⁺ effectively neutralize the negative charges on the surfaces of V₂O₅ NRs and GO nanosheets and bridge them during a coprecipitation process to form strongly bound V₂O₅ NR/GO assemblies. During the thermal annealing process at ${\sim}300~^{\circ}\text{C}$ in a N_2 atmosphere, GO is converted into rGO while the acetate anions are decomposed into gas products and released from the materials. At the meantime, some M2+ ions insert into V₂O₅ NRs, making them a layer-expanded disordered V₂O₅ material to improve the Zn²⁺ ion storage properties. With only Zn²⁺ ions present during coprecipitation, the produced Zn-V₂O₅ NR/rGO hybrid has an estimated elemental formula as Zn_{0.42}V₂O_{7.54} and presents a high reversible specific capacity of ${\sim}395~\text{mAh}~\text{g}^{-1}$ at 0.50 A g^{-1} current density (${\sim}1.3\text{C}$ rate) with nearly 100% CE, but the capacity retains only ~28% from cycle #50 to cycle #2000 at 4.0 A g⁻¹. The stability is significantly improved by mixing a fraction of \mbox{Mn}^{2+} ions with the \mbox{Zn}^{2+} ions during the coprecipitation process, which leads to a binary divalent metal ion-mediated hybrid (Mn + Zn)-V₂O₅ NR/ rGO. The elemental composition is determined to be Zn_{0.12}Mn_{0.14}V₂O_{7.16}. This approach sacrifices a small portion of the specific capacity for Zn²⁺ ion storage by incorporation of Mn²⁺ ions as stronger fixed pillars, ^{26,27} with a lower specific capacity of \sim 291 mAh g⁻¹ at 0.5 A g⁻¹. But, the rate performance is substantially improved, showing only a small decrease in the specific capacity to \sim 231 mAh g⁻¹ at 4.0 A g⁻¹. The long-cycling test at 4.0 A g⁻¹ shows a much-improved stability with a specific capacity retention of 77% from cycle #50 to cycle #2000 for $(Mn + Zn)-V_2O_5 NR/rGO$ in contrast to the 28% for Zn-V₂O₅ NR/rGO. This is benefited from the stronger binding of $\rm Mn^{2+}$ ions with the V₂O₅ host, which serve as more stable pillars to expand the V_2O_5 layers. ²⁶⁻²⁹ This strategy can be optimized in the future to achieve both high specific capacity and good long-cycling stability.

■ EXPERIMENTAL SECTION

The brief experimental procedures are described below. More details can be found in the Supporting Information (SI).

Material Synthesis. V₂O₅ NRs were synthesized using microwave-assisted exfoliation reported in our previous work. ²⁴ In brief, commercial orthorhombic α -V₂O₅ (bulk V₂O₅) powder was soaked in deionized (DI) water for about 4 h to facilitate intercalation of water molecules between the V₂O₅ layers. The soaked V₂O₅ powder was then transferred to a low-microwave-absorption solvent tetrahydrofuran (THF) and irradiated with microwave at a constant power of 300 W in a Discover SP microwave reactor (CEM, Matthews, NC). The temperature was ramped in ~9 min to reach 150 °C, and this setting was maintained for an hour. After the microwave reaction, the exfoliated V₂O₅ NRs (Figure S1a) were collected as a bright-yellow-colored supernatant and separated from the bulk V₂O₅ precipitate by centrifugation.

The V₂O₅ NR/rGO hybrid materials were prepared by divalent cation-mediated coprecipitation. Both the exfoliated V₂O₅ NRs (Figure S1a) and the commercial single-layer GOs (Figure S1b) were negatively charged in DI water and formed stable homogeneous suspensions due to electrostatic repulsion. After mixing 20% of GO nanoflakes and 80% of V2O5 NRs in water at a concentration of 1.63 mg/mL, they formed a stable, yellow-colored homogeneous binary suspension (Figure S1c). Then, 0.10 M zinc acetate or 0.10 M (Mn + Zn) acetate (containing 0.036 M Mn(II) acetate and 0.064 M Zn(II) acetate) was added dropwise to the mixed V2O5 NR and GO suspension to form a gray-yellow gel-like precipitate at the bottom of the glass vial, clearly separated from the clear water at the top (Figure S1d). The gel-like precipitates were collected and washed with DI water and then dried overnight on a hotplate at 70 °C to get a black coprecipitated powder (Figure S1e). The amount of the salts was adjusted to provide sufficient divalent metal ions (M²⁺) to bind V₂O₅ NRs and GO nanosheets, while the extra ions were washed off. The dried Zn-V₂O₅ NR/GO and (Mn + Zn)-V₂O₅ NR/GO precipitates were then annealed at 300 °C in a N2 atmosphere for 2 h (at an initial ramping rate of 10 °C/min) to reduce GO into rGO and decompose M(CH₃COO)₂ into MO and gas products (dominated by CO₂).²⁵ Temperatures higher than 300 °C were avoided since it led to reduction of metal oxides into metallic metal due to a carbothermal reaction with rGO. The obtained hybrid materials are referred to as Zn-V₂O₅ NR/rGO and (Mn + Zn)-V₂O₅ NR/rGO or generally as M-V2O5 NR/rGO.

Material Characterization. Raman spectroscopy analysis was performed with a DXR Raman microscope (Thermo Fisher Scientific, Madison, WI) with a 532 nm laser at 10 mW, under a 10× objective

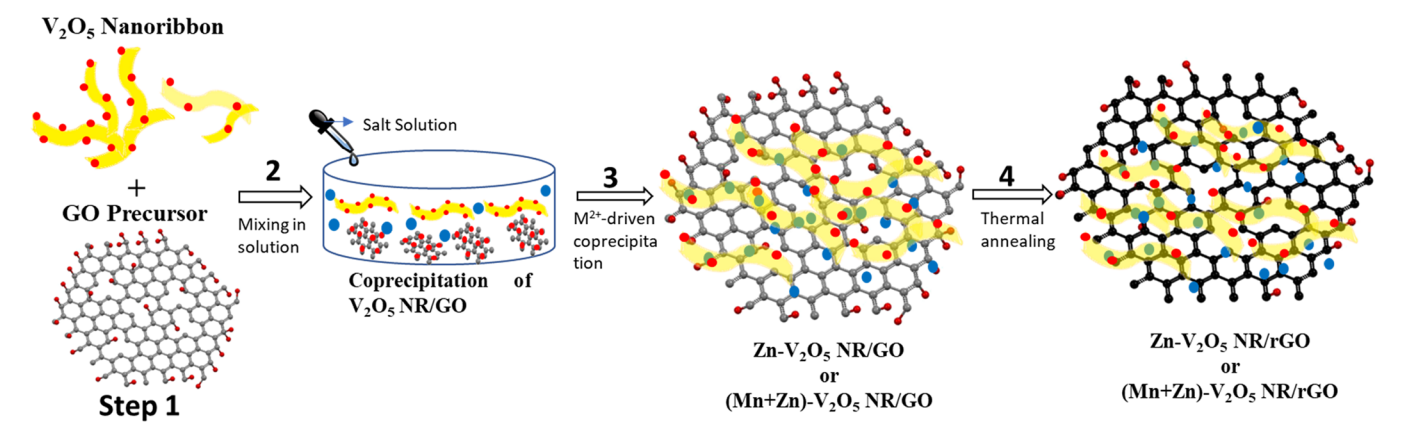


Figure 1. Schematic illustration of the synthesis of V_2O_5 NR/rGO hybrids by coprecipitation. Step 1: V_2O_5 NRs and GO precursors are dispersed in water to form stable suspensions by ultrasonication. Step 2: The mixed V_2O_5 and GO precursors remain as a homogeneous suspension due to electrostatic repulsion. Step 3: Zinc acetate or manganese acetate solutions are added dropwise to coprecipitate the negatively charged V_2O_5 NRs and GO nanosheets into a gel-like precipitate, which is collected and dried by heating for 6 h at 70 °C on a hotplate. Step 4: The dried M- V_2O_5 NR/GO is further annealed in a tube furnace at 300 °C for 2 h in a N_2 atmosphere to convert GO to rGO and form the hybrid material of M- V_2O_5 NR/rGO.

lens with a slit width of 50 μ m. The powder X-ray diffraction (XRD) study was done with a D8 Advance diffractometer (Bruker Corporation, Karlsruhe, Germany) with a Cu Klpha radiation of wavelength 0.15418 nm. The surface composition and chemical environment of V₂O₅/rGO hybrids were analyzed using a PHI 5000 Versa X-ray Photoelectron spectroscopy (XPS) system (Chanhassen, MN) with a monochromatized Al K α source (1486.7 eV). The transmission electron microscopy (TEM) images were obtained using a Philips CM 100 with a tungsten source and a high tension of 100 kV. The field emission scanning electron microscopy (FESEM) images were obtained using a Topcon/ISI/ABT DS 130F FESEM microscope (Akashi Beam Technology Corporation, Tokyo, Japan). Thermogravimetric analysis (TGA) was carried out with a TGA Q50 system (TA Instruments, Waters LLC, New Castle, DE) from room temperature to 550 °C in the air. The zeta potential measurements were carried out using a ZetaPALS Zeta Potential analyzer (Brookhaven Instruments Corporation, NY, USA).

Electrochemical Characterization. A slurry was prepared by mixing the active material (V2O5 NR/rGO, Zn-V2O5 NR/rGO, and (Mn + Zn)-V₂O₅ NR/rGO), carbon additive (Super-P), and a poly(vinylidene fluoride) (PVDF) binder at a weight ratio of 8:1:1 with approximately 150 μ L of N-methyl-2-pyrrolidone (NMP) as the solvent. The homogeneous slurry was then brush-coated onto a 0.10 mm thick titanium disk with a diameter of 15 mm for AZIB half-cell tests. The coated electrodes were vacuum-dried at 110 °C overnight and used as the cathode in AZIBs. A Zn disk (Sigma Aldrich, St. Louis, MO) of 0.25 mm thickness and 15 mm diameter was used as the anode. Commercially purchased glass fiber disk (El-Cell, Hamburg, Germany) of 18 mm diameter and 0.65 mm thickness was used as the separator. The electrode/separator stacks were assembled into stainless steel coin cells (CR 2025, MTI Corporation, Richmond, CA, USA) in an ambient atmosphere with 2.0 M ZnSO₄ aqueous solution as the electrolyte. The AZIB cells were tested in a voltage window of 0.20-1.80 V with a Neware battery testing system (Shenzhen, China).

■ RESULTS AND DISCUSSION

Synthesis Design. The synthesis of M-V₂O₅ NR/rGO hybrids is illustrated in Figure 1. Over the past decade, the V₂O₅ nanostructures have been investigated widely as efficient electrode materials for EES such as LIBs,³⁰ supercapacitors,³¹ sodium ion batteries,³² and AZIBs.³³ It has been proven that V₂O₅ nanostructures such as nanorods,⁵ nanowires,³⁴ nanospheres,³³ and nanoribbons^{35,36} present higher specific capacity and better stability compared to the bulk counterparts. In the

past, V₂O₅ nanostructures were synthesized with solvothermal methods, 35,36 template-based methods, 37 and electrochemical deposition. 38 Among them, the hydrothermal technique is considered easier and effective. In this work, we emphasize on the sustainable and scalable material synthesis toward future AZIBs. We demonstrate a facile coprecipitation method by self-assembly of dissimilar V₂O₅ NRs (made by the rapid microwave-exfoliated process) and GO nanosheets into intimate hybrid materials. A small amount of water molecules was first intercalated between the V₂O₅ layers by soaking bulk V₂O₅ powders in distilled water and then subjected to microwave heating. The microwave-assisted synthesis is known as a faster and more environmentally friendly technique compared to conventional hydrothermal techniques.²⁴ In this study, a unique specific heating method provides additional advantages. The microwave absorbing capability of a material is defined by its dielectric properties, i.e., the loss tangent value $(\tan \delta = \varepsilon''/\varepsilon')$, where ε' and ε'' represent the time-dependent polarizability and permittivity, respectively. The pre-intercalated water molecules (with $tan\delta = 0.123$) in the V_2O_5 structure has a much larger tan δ value than THF solvent $(\tan \delta = 0.047)^{.39}$ The faster heating to the intercalated water molecules by the microwave leads to breaking and separating the V₂O₅ layers, which are bonded by weak van der Waals interaction, thus exfoliating the bulk α -orthorhombic V_2O_5 structure into V₂O₅ NRs.

The surface of the as-exfoliated 1D V₂O₅ NRs and 2D GO nanosheets is negatively charged, showing zeta potentials of -32.16 and -31.55 mV, respectively, in DI water (Table S1). Each material forms a homogeneous suspension, as shown in Figure S1a,b, and remains as a stable homogeneous suspension after mixing (Figure S1c) due to their repulsive electrostatic interactions. This prevents them from assembling into intimate hybrid materials. However, they easily coprecipitate into a gellike material (Figure S1d) after addition of divalent metal cations (such as Zn²⁺ and Mn²⁺), which neutralize the negative charges and assemble V₂O₅ NRs and GO nanosheets together, as schematically illustrated in Figure 1. This forms a hybrid material with V2O5 NRs uniformly anchored on GO nanosheets. The coprecipitated V₂O₅ NR/GO hybrids were annealed in a N2 atmosphere at 300 °C to convert the GO into less defective rGO for higher electrical conductivity. The M²⁺

cations not only hold V_2O_5 NRs and GO nanosheets together but also intercalate into a V_2O_5 NR framework when the salts decompose into metal oxides during thermal annealing, which expand the V_2O_5 layers and provide continuous ion conduction pathways in the assembly.

Morphological Characterization. TEM was performed to investigate the morphology and crystal structure of V_2O_5 NRs, $Zn-V_2O_5$ NR/rGO, and $(Mn + Zn)-V_2O_5$ NR/rGO. Figure 2a,b shows the representative TEM images of bare rGO

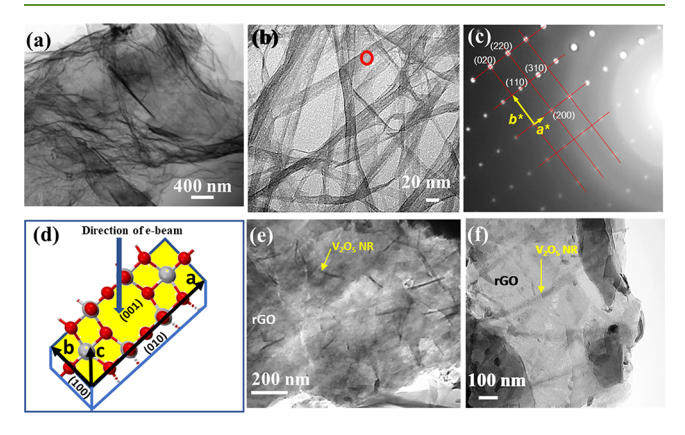


Figure 2. TEM images of (a) bare rGO and (b) as-exfoliated V_2O_5 NRs. (c) Selected area electron diffraction (SAED) pattern of the V_2O_5 NR red-circled in panel (b) and the (hk0) index according to an orthorhombic α - V_2O_5 crystal structure (based on the standard pattern of JCPDS: 41-1426) with the (001) plane perpendicular to the electron beam. (d) Illustration of the crystal orientation of the V_2O_5 NRs. TEM images of the coprecipitated hybrid materials of V_2O_5 NRs on rGO nanosheets in the form of (e) Zn- V_2O_5 NR/rGO and (f) (Mn + Zn)- V_2O_5 NR/rGO.

and as-exfoliated V_2O_5 NRs, respectively. The morphology of the bare rGO resembles the typical nanoflake structure with many long (over several microns) and curved wrinkles on the surface due to its softness. The TEM image of the microwave-exfoliated V_2O_5 NRs in Figure 2b shows the random stack of shorter ribbon-like structures with a width of 10–30 nm and a length of several microns. The V_2O_5 NR morphology is clearly different from that of the bulk V_2O_5 crystalline powder as compared in Figure S2.

Interestingly, the selected area electron diffraction (SAED) pattern in Figure 2c, measured from the red-circled area in Figure 2b, shows extended sharp diffraction spots forming a well-defined rectangular lattice matching the 2D in-plane diffraction of the (001) plane of the orthorhombic α -V₂O₅ crystals. For clarity, only the SAED pattern in a darker area off from the direct beam spot is shown in Figure 2c. The SAED pattern clearly reveals that the exfoliated V₂O₅ NRs preserve the orthorhombic α -V₂O₅ structure of the starting bulk crystal, 40,41 which is illustrated in Figure S3 with three orthogonal lattices: a = 11.516 Å, b = 3.566 Å, and c =4.373 Å (based on JCPDS: 41-1426). The selected V_2O_5 NR in Figure 2b,c predominantly lies flat on the TEM grid with the crystal plane (001) perpendicular to the electron beam. Thus, all SAED spots can be indexed as (hk0) of the bulk orthorhombic α-V₂O₅ crystal. The full raw SAED pattern in Figure S4a and the enlarged area near the (000) spot in Figure S4b reveal the same information. Further analysis of the orientation of the rectangular SAED pattern in the text following Figure S4 in the SI reveals that the (010) direction

(lattice b) of this V_2O_5 NR is perpendicular to the long ribbon axis, while the (100) direction (lattice a) is along the long ribbon axis, as illustrated in Figure 2d. Furthermore, the SAED pattern shows systematic variations among the (hk0) spots, with some spots (such as (200), (020), (110), (220), etc.) appearing bright while others (such as (100), (010), (120), (210), etc.) being dark. These are consistent with the form factors of the large orthorhombic α -V₂O₅ unit cell, as shown in the JCPDS: 41-1426 file. Clearly, the exfoliated V₂O₅ NRs preserve the orthorhombic α -V₂O₅ crystal structure 40,41 and are aligned in specific crystal orientations. Figure 2e,f shows the representative TEM images of Zn-V₂O₅ NR/rGO and (Mn + Zn)-V₂O₅ NR/rGO hybrids, respectively. The V₂O₅ NRs (indicated by the yellow arrows) can be seen sandwiched between rGO nanosheets in the hybrid structure, further demonstrating the successful assembly of V2O5 NRs on rGO nanosheets. The V₂O₅ NRs seem to break into shorter rigid pieces (with an average length of ~300 nm) after thermal annealing.

The morphologies of as-exfoliated V_2O_5 NR aggregates and the coprecipitated V_2O_5 NR/rGO hybrids are quite different as illustrated by FESEM. As shown in Figure 3a–c, the V_2O_5 NRs

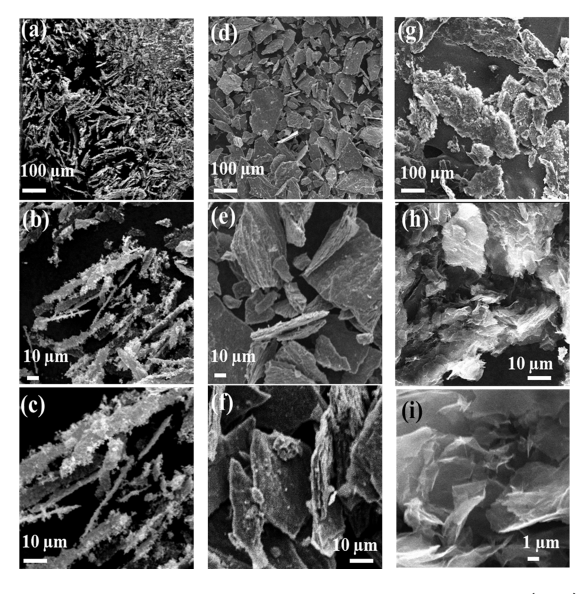


Figure 3. FESEM images at low to high magnifications of (a–c) as-exfoliated V_2O_5 NRs, (d–f) Zn- V_2O_5 NR/rGO, and (g–i) (Mn + Zn)- V_2O_5 NR/rGO.

aggregate into rigid fibers from several to tens of microns in length and 1–10 microns in width, which are much larger than the dispersed $\rm V_2O_5$ NRs under TEM in Figure 2b. In contrast, the FESEM images of Zn-V_2O_5 NR/rGO in Figure 3d–f present flat plate-like structures with the thickness ranging from 1 to 5 μm and lateral size up to 50 μm . The large plate size and thickness indicate that they likely consist of a stack of many V_2O_5 NRs and rGO nanosheets during the self-assembly process. The Zn-V_2O_5 NR/rGO hybrid plates appear to be more rigid than the GO nanosheets in Figure 2a. The FESEM images of (Mn + Zn)-V_2O_5 NR/rGO in Figure 3g–i show much thinner (<1 μm) and wrinkled plates compared to Zn-V_2O_5 NR/rGO. The surface is rougher, indicating a more disordered structure than Zn-V_2O_5 NR/rGO. Incorporating mixed Mn^2+ and Zn^2+ cations seems to disrupt the tight

packing of V₂O₅ NR/rGO, which could facilitate faster ion transport.

Structural Characterization. The microstructures of V_2O_5 NRs, $Zn-V_2O_5$ NR/rGO, and $(Mn+Zn)-V_2O_5$ NR/rGO are further studied using Raman spectroscopy and XRD. Figure 4a presents the Raman spectra of bulk V_2O_5 (black),

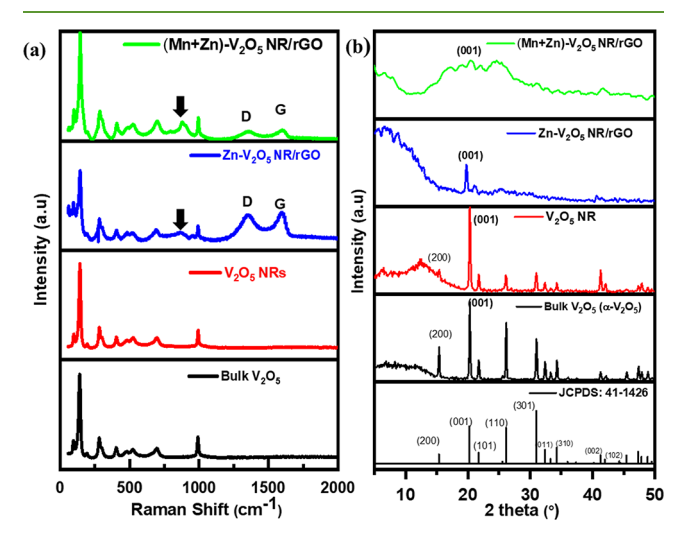


Figure 4. (a) Raman spectra and (b) powder XRD spectra of Zn- V_2O_5 NR/rGO (blue) and (Mn + Zn)- V_2O_5 NR/rGO (green) in comparison to the control samples of V_2O_5 NRs (red) and bulk V_2O_5 powder (black). The bottom part of panel (b) is the standard pattern of orthorhombic α- V_2O_5 crystal (JCPDS: 41-1426).

V₂O₅ NR (red), Zn-V₂O₅ NR/rGO (blue), and (Mn + Zn)- V_2O_5 NR/rGO (green). The Raman spectrum of V_2O_5 NR matches well with that of the commercial V₂O₅ powder, suggesting that the microwave-assisted exfoliation process does not disrupt the local crystal structure of $\alpha\text{-V}_2\text{O}_5$. The Raman spectra of all samples show distinct peaks at 140.9, 281.6, 403.1, 529.4, 695.3, and 991.3 cm⁻¹, which are attributed to the -O-V-O-V- stretching, $V-O_1$ bending, V-O₃ bending, V-O₂ stretching, V-O₃ stretching, and V-O₁ stretching of the V_2O_5 layers in the α - V_2O_5 structure. ^{24,42,43} In addition, the Raman spectra of Zn-V₂O₅ NR/rGO and (Mn + Zn)-V₂O₅ NR/rGO show a broad peak around 870 cm⁻¹ (marked with the arrows) that can be attributed to the presence of multiple oxidation states of vanadium due to the intercalation or surface binding of Zn²⁺ and Mn²⁺ cations.⁴⁴ The Raman spectra of Zn-V₂O₅ NR/rGO and (Mn + Zn)-V₂O₅ NR/rGO also show two major peaks at 1350 and 1598 cm⁻¹, attributed to the D and G bands of the rGO nanosheets, originating from the vibrational modes of sp³ carbon at the defect sites and the in-plane vibration of sp²-bonded carbon atoms. The low I_D/I_G ratios, 0.83 in Zn-V₂O₅ NR/rGO and 0.92 in (Mn + Zn)-V₂O₅ NR/rGO, suggest the successful conversion of GO to rGO, with some defects remaining in the sp² lattice upon removal of the oxygenated functional groups by thermal annealing.45

The XRD spectra of bulk V_2O_5 (black), V_2O_5 NRs (red), Zn- V_2O_5 NR/rGO (blue), and (Mn + Zn)- V_2O_5 NR/rGO (green) are compared with the JCPDS: 41-1426 standard pattern of the orthorhombic α - V_2O_5 structure (black) in Figure 4b. The XRD spectra of bulk V_2O_5 powder and V_2O_5 NRs show very similar well-defined sharp peaks exactly matching the α - V_2O_5 standard pattern (JCPDS: 41-1426), suggesting that V_2O_5 NRs preserve the bulk orthorhombic

crystal structure, 46 consistent with the SAED in Figure 2c. The (001) diffraction peak of V₂O₅ NRs is relatively more intense than the other peaks, such as (110) and (301), suggesting the higher order stacking of V₂O₅ layers in the (001) direction.⁴⁷ The d-spacings of the commercial bulk V₂O₅ and exfoliated V_2O_5 NRs are the same (0.437 nm) based on the (001) peak at $2\theta = 20.26^{\circ}$. The XRD spectrum of Zn-V₂O₅ NR/rGO shows only two weak diffraction peaks at the 2θ values of 19.80 and 21.05°, attributed to the (001) and (101) diffraction of V₂O₅. The absence of other diffraction peaks may be due to the disordering caused by intercalation of Zn2+ ions in the V₂O₅ structure. This is further supported by the shift of the (001) peak from 20.26° in the exfoliated V₂O₅ NRs to a lower value of 19.80° in Zn-V₂O₅ NR/rGO, suggesting a slightly larger d-spacing of 0.447 nm. In contrast, the XRD spectrum of (Mn + Zn)-V₂O₅ NR/rGO only shows uncharacteristic broad peaks, which might contain a peak around 20° corresponding to V₂O₅. These broad peaks reflect a much higher disordering in V₂O₅ NRs owing to the intercalation of mixed Mn²⁺ and Zn²⁺ ions, which is consistent with the FESEM images in Figure 3g-i. It is noted that the weak broad XRD peaks below $\sim 15^{\circ}$ in 2θ angle are obscured by the background from the plastic sample holder (as shown in Figure S5) and should be ignored.

Composition Analysis. The chemical composition of bulk V_2O_5 , V_2O_5 NRs, $Zn-V_2O_5$ NR/rGO, and $(Mn+Zn)-V_2O_5$ NR/rGO were investigated using XPS analysis in binding energy (BE) ranges for V 2p (512–528 eV), O 1s (528–535 eV), C 1s (280–294 eV), Zn 2p (1010–1050 eV), and Mn 2p (638–662 eV), which are presented in Figures S6 and S7 in the SI. The BE peak positions and relative atomic percentage (at %) of the elements are summarized in Table S2.

In summary, the vanadium atoms in all V₂O₅ samples are dominated by V⁵⁺ (>82% of all V atoms) with a small portion present as V⁴⁺. The percentage of V present as V⁴⁺ in V₂O₅ NRs and M-V₂O₅ NR/rGO hybrids is about 12-17%, slightly higher than that in the bulk V₂O₅ powder (8.9%). Compared to V_2O_5 NRs, the V^{4+} $2p_{3/2}$ peak slightly shifts up by 0.29 and $0.37 \text{ eV in Zn-V}_2O_5 \text{ NR/rGO}$ and $(\text{Mn} + \text{Zn})\text{-V}_2O_5 \text{ NR/rGO}$, respectively, indicating the electron transfer from V⁴⁺ centers to the intercalated ions (Zn2+ and Mn2+) in the coprecipitated M-V₂O₅ NR/rGO hybrids. The presence of the V⁴⁺ oxidation state has been observed to improve the electrochemical performance owing to the lower polarization and faster ion diffusion. However, there is no shift in the V^{5+} 2p_{3/2} peak, suggesting that the pre-intercalated Zn²⁺ and Mn²⁺ ions do not bind on the V5+ centers, leaving a major part of the V2O5 host available for reversible Zn2+ ion storage.

The Zn 2p peaks of Zn-V₂O₅ NR/rGO in Figure S7d can be deconvoluted into three pairs of doublets positioned at (1020.21 and 1044.06 eV), (1022.06 and 1045.36 eV), and (1023.5 and 1047.0 eV), corresponding to weakly bound Zn²⁺ from acetate salt and more strongly bound Zn²⁺ in V₂O₅ and ZnO, respectively. The relative at % values are 10.8, 76.4, and 12.8%, respectively. The Zn 2p peaks of (Mn + Zn)-V₂O₅ NR/rGO can be fitted in the same way except that the Zn at % in the acetate salt increased to 40.2% due to incorporation of Mn²⁺ ions (see discussion in page S14 of the SI). The Mn 2p spectrum of (Mn + Zn)-V₂O₅ NR/rGO in Figure S7f shows three pairs of 2p_{3/2} and 2p_{1/2} peaks at (640.57 and 651.81 eV), (642.07 and 653.51 eV), and (646.70 and 656.20 eV), suggesting that the Mn ions are present in three oxidation states, i.e., Mn²⁺ (9.2% of all Mn atoms), Mn³⁺ (41.5% of all

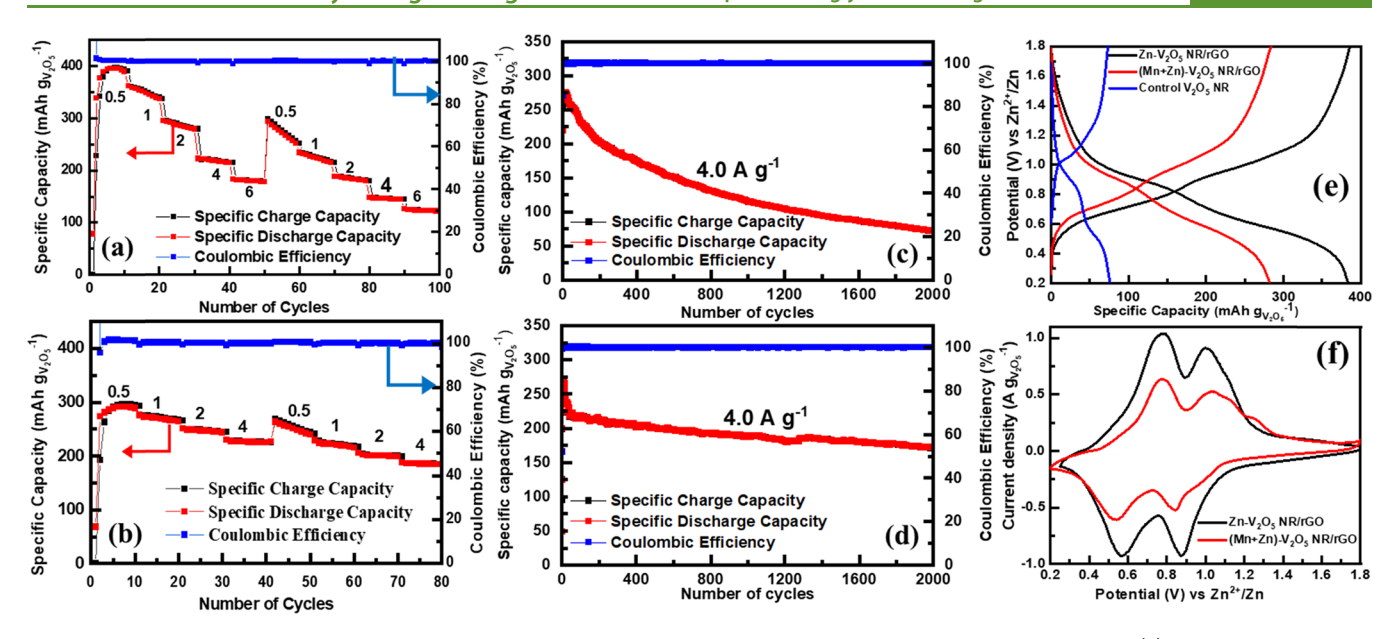


Figure 5. Galvanostatic charge—discharge characterization of the aqueous ZIBs in the potential window of 0.20-1.80~V. (a) The rate performance plots measured sequentially at different current densities (i.e., 0.5, 1.0, 2.0, 4.0, and $6.0~A~g^{-1}$) for the (a) Zn-V₂O₅ NR/rGO cathode and (b) (Mn + Zn)-V₂O₅ NR/rGO cathode. Stability tests over 2000 cycles of the aqueous ZIBs at a fixed current density of $4.0~A~g^{-1}$ with the (c) Zn-V₂O₅ NR/rGO cathode and (d) (Mn + Zn)-V₂O₅ NR/rGO cathode. The current densities are calculated based on the total mass of M-V₂O₅ NR/rGO materials, while the specific capacities are calculated based on the mass of active M-V₂O₅ NRs derived from TGA analysis (Table S3). (e) Comparison of galvanostatic charge—discharge profiles of the AZIBs at $0.50~A~g^{-1}$ with the cathode made of V₂O₅ NRs (blue), (Mn + Zn)-V₂O₅ NR/rGO (red), and Zn-V₂O₅ NR/rGO (black). (f) Comparison of CV curves of the AZIBs made of Zn-V₂O₅ NR/rGO (black) and (Mn + Zn)-V₂O₅ NR/rGO (red) cathodes at a scan rate of $0.50~mV~s^{-1}$.

Mn atoms), and Mn^{4+} (49.3% of all Mn atoms), respectively. Clearly, a large portion of Mn^{2+} is oxidized to higher valence states during the thermal annealing process, which is expected to bind more strongly with the V_2O_5 host and rGO.

Table S2 summarizes the estimated atomic percentages and/ or relative ratios of different elements based on the XPS spectra. The atomic ratios of V to O are estimated to be 1:2.7, 1:3.13, 1:3.77, and 1:3.58 in bulk V₂O₅, V₂O₅ NRs, Zn-V₂O₅ NR/rGO, and (Mn + Zn)-V₂O₅ NR/rGO, respectively. The V:O ratio in all these samples is lower than the stoichiometric ratio of 1:2.5 for pure V₂O₅. The extra O atoms can be attributed to absorption of water from environmental moisture and residue O in rGO. V2O5 NRs present a higher O content than the bulk V₂O₅ due to the larger specific surface area. The Zn-V₂O₅ NR/rGO and (Mn + Zn)-V₂O₅ NR/rGO hybrids present further increased O atoms, which can be attributed to the formation of metal oxides during the coprecipitation and annealing processes as well as oxygen-containing groups in rGO. The elemental formula of Zn-V₂O₅ NR/rGO and (Mn + $Zn)\text{-}V_2O_5$ NR/rGO are estimated as $Zn_{0.42}V_2O_{7.54}$ and Zn_{0.12}Mn_{0.14}V₂O_{7.16}, respectively, based on the atomic ratios listed in Table S2. These are consistent with the composition of intercalated metal ions in expanded V2O5 materials in literature, i.e., $M_xV_2O_5$ with x = 0.17 - 0.44. 18,19,27,50

TGA was carried out from room temperature to 550 °C in air at a heating rate of 10 °C/min to derive the weight percentages (wt %) of V_2O_5 NRs and rGO in the composites. Figure S8a presents the comparison of the TGA curves of V_2O_5 NRs, bare rGO, Zn- V_2O_5 NR/rGO, and (Mn + Zn)- V_2O_5 NR/rGO, and Figure S8b shows those of two control samples. V_2O_5 NRs show almost a flat line with a negligible weight loss up to 550 °C. In contrast, bare rGO shows a rapid weight loss (by 89.84 wt %) from 400 to 490 °C due to oxidation of rGO into CO₂. Based on these properties, the wt

% of rGO and metal oxide in the M-V₂O₅ NR/rGO hybrids are derived and listed in Table S3, with rGO consisting of 21.66 wt % in Zn-V₂O₅ NR/rGO and 12.98 wt % in (Mn + Zn)-V₂O₅ NR/rGO.

Electrochemical Characterization. The Zn²⁺ ion storage properties of Zn-V₂O₅ NR/rGO and (Mn + Zn)-V₂O₅ NR/ rGO cathodes are systematically investigated using galvanostatic charge-discharge tests for rate performance and longterm cycling evaluation. Cyclic voltammetry (CV) tests were carried out to understand the mechanisms. The rate performance of Zn-V₂O₅ NR/rGO as the AZIB cathode is shown in Figure 5a, with the current density sequentially set at 0.50, 1.0, 2.0, 4.0 and 6.0 A g^{-1} (based on the total mass of Zn-V₂O₅ NR/rGO) in the voltage window of 0.20 V-1.80 V. Ten charge-discharge cycles are applied at each current density value. The starting current density (0.50 A g⁻¹) is about 1.7C rate based on a theoretical capacity of 294 mAh g⁻¹ (one Zn²⁺ ion per V₂O₅). (Mn + Zn)-V₂O₅ NR/rGO is characterized in the same way except that the current density of 6 A g⁻¹ is not applied. The specific capacity for the hybrid materials is calculated using the mass of the active Zn²⁺ storage materials (i.e., M-V₂O₅) based on TGA. The small rGO wt % was neglected since its overall contribution to the storage capacity is less than 1% (to be discussed later).

The rate performance of Zn-V₂O₅/rGO in Figure 5a shows that it quickly increases to a very high specific capacity of 395 mAh g⁻¹ after the initial four cycles at a starting current density (0.50 A g⁻¹), which is equivalent to \sim 1.34 Zn²⁺ ion per V₂O₅. However, as the current density increases to 1.0, 2.0, 4.0, and 6.0 A g⁻¹, the specific capacity decreases to about 351, 287, 216, and 185 mAh g⁻¹, respectively, corresponding to about 11, 27, 45, and 53% drop from the specific capacity at 0.50 A g⁻¹. Also, when the measurement is switched back to 0.5 A g⁻¹ after completing the 50 cycles of the first rate performance

sequence, the specific capacity drops to 293 mAh g⁻¹. The CE is 99% to 100% in all cycles except in the initial four cycles, indicating the high reversibility of $\rm Zn^{2^+}$ ion storage. The rate performance of the (Mn + Zn)-V₂O₅ NR/rGO cathode in Figure 5b shows a slightly lower average specific capacity of 291 mAh g⁻¹ at 0.5 A g⁻¹. The average specific capacity slightly decreases to 271, 248, and 231 mAh g⁻¹ as the current density is increased to 1.0, 2.0, and 4.0 A g⁻¹, respectively. The magnitude of the decrease at higher rates is significantly smaller than that of Zn-V₂O₅/rGO. For example, at 4.0 A g⁻¹, the specific capacity drops by 45% from that at 0.5 A g⁻¹ with Zn-V₂O₅/rGO while it only drops by 21% with (Mn + Zn)-V₂O₅ NR/rGO. A higher capacity retention of over 84% is also obtained when switching back to a low current density of 0.50 A g⁻¹ at the 41st cycle.

The performances of Zn-V₂O₅ NR/rGO and (Mn + Zn)-V₂O₅ NR/rGO at the fixed current density of 4.0 A g⁻¹ over 2000 cycles are shown in Figure 5c,d, respectively, while the first 50 cycles are shown in Figure S13a,b. The Zn-V₂O₅ NR/ rGO cathode exhibits a high specific capacity \sim 250 mAh g⁻¹ in the first cycle, slightly increases to \sim 276 mAh g⁻¹ in the 15th cycle, and stabilized at \sim 254 mAh g⁻¹ in the 50th cycle. It then continuously decreases to 72 mAh g⁻¹ in cycle #2000 (retaining 28% of the value at cycle #50). This poor cycling stability is consistent with the fast fading in at low current densities in Figure 5a. In contrast, the (Mn + Zn)-V₂O₅ NR/ rGO AZIB involves a slower activation process with the specific capacity steadily increasing from \sim 50 mAh g⁻¹ in cycle #1 to 272 mAh g^{-1} in cycle #10. It slightly drops and is stabilized at 222 mAh g⁻¹ in cycle #50. Overall, the (Mn + Zn)-V₂O₅ NR/rGO AZIB shows a much better stability, retaining 77% capacity from cycle #50 to cycle #2000. The slower activation of (Mn + Zn)-V₂O₅ NR/rGO can be attributed to the reconfiguration of Zn²⁺ ion diffusion pathways in this hybrid material. It is worth noting that both Zn-V₂O₅ NR/rGO and $(Mn + Zn)-V_2O_5$ NR/rGO cathodes show good reversibility with a CE of 99-100% during the long cycles. Zn-V₂O₅ NR/rGO shows a higher specific capacity than the theoretical value at charge-discharge densities below 1 A g⁻¹, which can be attributed to the reversible extraction/insertion of the pre-inserted Zn²⁺ ions (introduced during coprecipitation and annealing), which are weakly bound to the V₂O₅ host. In contrast, Mn²⁺ ions in (Mn + Zn)-V₂O₅ NR/rGO are strongly bound to the V2O5 host and are not extracted during charging processes. These pre-occupy some sites for Zn²⁺ ion intercalation and lower the specific capacity in (Mn + Zn)-V₂O₅ NR/rGO. It takes longer time to open up pathways for Zn²⁺ ion insertion/extraction.⁵¹ Interestingly, a previous study of AZIBs with Na+ ion stabilized V2O5 nanowires as the cathode showed the similar slow activation process (taking more than 500 cycles) but better capacity retention (over 93% after 1000 cycles). 19 The use of 3 M Zn(CF₃SO₃)₂ aqueous electrolyte in that study may have helped to improve the cycle stability, which is worthy of a study in the future.

From the above discussion, $Zn-V_2O_5$ NR/rGO can provide higher initial specific capacity but the repeated extraction/insertion of the bridging Zn^{2+} ions cause disruption to the structure of the hybrid material, leading to rapid capacity fading. On the other hand, $(Mn + Zn)-V_2O_5$ NR/rGO consists of an increased V^{4+}/V^{5+} ratio, which improves the redox kinetics of Zn^{2+} ions. The Z^{5+} ions (with Z^{5+} in Z^{5+} and Z^{5+} ions (with Z^{5+} in Z^{5+

electronic transport, leading to better rate performance and higher capacity retention.⁵¹ It has been reported that even the divalent Mn^{2+} ions serve as stable pillars in expanded V_2O_5 layers for Zn^{2+} ion storage. The dominating higher oxidation states of Mn³⁺ (42%) and Mn⁴⁺ (49%) in the (Mn + Zn)-V2O5 NR/rGO hybrid, as revealed by XPS analyses, may bind even stronger with V₂O₅ layers and block some of the active sites for Zn²⁺ ions, thus causing a deduction in the specific capacity during charge-discharge cycles. The magnitude of the capacity drops from Zn-V₂O₅NR/rGO to $(Mn + Zn)-V_2O_5NR/rGO$ at the initial low rate of 0.5 A/g is ~104 mAh/g, corresponding to ~0.36 Zn^{2+} per V_2O_5 . This is larger than 0.14 Mn in the formula $Zn_{0.12}Mn_{0.14}V_2O_{7.16}$. It is likely that they blocked the intercalation of more Zn^{2+} ions than the stoichiometric factor and caused the larger capacity drop, which was partially regained by activation in following cycles. In the future, a method to control Mn at +2 states or using other large divalent ions may free up more sites for higher Zn2+ ion storage.

For comparison, the rate performance and charge—discharge curves of control V₂O₅ NRs and bulk V₂O₅ are shown in Figure S9. The specific capacity of Zn²⁺ storage in the bulk V_2O_5 is negligible (<15 mAh $g^{-1}).$ The V_2O_5 NR offers ${\sim}80$ mAh g^{-1} at 0.5 A g^{-1} , much higher than the bulk V_2O_5 , but is three to five times smaller than M-V₂O₅ NR/rGO hybrids. Interestingly, at the same current density, the specific capacity keeps rising, which may be due to slower activation of the crystalline V₂O₅ NRs. Similarly, the rate performance tests of physically mixed V₂O₅ NRs and rGO (without incorporation of the divalent metal cations) are compared with the bare rGO in Figure S10. The bare rGO in Figure S10a shows a negligible specific capacity below 12 mAh g $^{-1}$, which is only \sim 3% of that of Zn-V₂O₅ NR/rGO. It clearly explains that the Zn $^{2+}$ ion storage in the hybrid materials is dominated by the V₂O₅ NRs. The physically mixed V₂O₅ NR and rGO shows an initial specific capacity of 78 mAh g⁻¹ at 0.5 A g⁻¹, which is comparable to that of the bare V2O5 NR in Figure S9a (with the super-P additive) but decreases faster as the current density is raised. Clearly, simply mixing V2O5 NRs and rGO is not efficient to improve the Zn2+ ion storage properties. The divalent metal cation-mediated coprecipitation is necessary in creating an intimate hybrid material to provide the much higher specific capacity in Zn-V₂O₅ NRs/rGO (by 4.9 times) and $(Mn + Zn)-V_2O_5$ NRs/rGO (by 3.7 times).

For further comparison, the Na⁺ ion expanded sample, i.e., Na-V₂O₅ NR/rGO, was also prepared using similar coprecipitation in 0.20 M sodium acetate and fully characterized by Raman spectroscopy, TGA, and XRD (Figure S11). As shown in Figure S11a, the mixture produces a green-yellow gel-like precipitate. The supernatant has a brown color, indicating the presence of suspended GO. In contrast, it forms a clear supernatant when using 0.10 M divalent cations (such as Zn²⁺ and Mn²⁺) in Figure S1d. The rGO mass percentage in the annealed Na-V2O5 NR/rGO composite is also much lower, at about 5.6%. The XRD of Na-V₂O₅ NR/rGO is very similar to pristine V₂O₅ NRs. Clearly, monovalent ions are not effective in coprecipitating V₂O₅ NRs and GOs compared to divalent cations and have little disruption to the crystalline structure of V₂O₅ NRs. The rate performance of Na-V₂O₅ NR/rGO shows a lower specific capacity of 243-269 mAh g⁻¹ at a low rate of 0.5 A g⁻¹ but drops much faster as the charge-discharge rate is increased, down to nearly zero at 6 A g⁻¹ (Figure S12a,b). The stability in long cycling at 4 A g⁻¹ is decent after the initial

activation (Figure S12a,b) but mostly due to the fact that only a small amount of Zn^{2+} ions is intercalated, as reflected by a low specific capacity of 20–30 mAh g^{-1} .

The galvanostatic charge-discharge profiles of Zn-V₂O₅ NR/rGO and (Mn + Zn)-V₂O₅ NR/rGO are compared with pristine V₂O₅ NRs in Figure 5e. The shapes look similar, showing two sloped plateaus in ranges of 1.0-0.8 and 0.7-0.4 V during discharging, indicating similar electrochemical kinetics, but there are large differences in the Zn²⁺ ion storage capacities among these materials. The galvanostatic chargedischarge profiles at different cycles during the long cycling of $Zn-V_2O_5$ NR/rGO (Figure 5c) and (Mn + Zn)- V_2O_5 NR/ rGO (Figure 5d) are shown in Figure S13c,d. The curves maintain the same features during the cycling, but the specific capacity of Zn-V₂O₅ NR/rGO quickly reaches stabilization in the second cycle, maintains at this level for about 50 cycles, and then monotonically decreases in long cycling. In contrast, (Mn + Zn)-V₂O₅ NR/rGO starts at a much lower specific capacity, which slowly increases in the initial 10 cycles and becomes stabilized from cycle #11 to cycle #50, consistent with Figure S13c,d.

The CV curves of Zn- V_2O_5 NR/rGO and (Mn + Zn)- V_2O_5 NR/rGO in Figure 5f show two distinct pairs of peaks centered around 0.95 and 0.65 V, respectively, which are attributed to the two-step redox reactions well-known in AZIBs, ²⁷ correlated well with the voltage plateaus in the charge-discharge curves. The CV of Zn-V₂O₅ NR/rGO shows higher peak currents due to the larger Zn²⁺ storage capacity. The separation in the peak potentials of each redox wave pair is larger than 200 mV, indicating a high energy barrier of Zn2+ ion insertion/ extraction, which needs to be improved. The CV curves of the initial three cycles of Zn-V₂O₅ NR/rGO and (Mn + Zn)- V_2O_5 NR/rGO (Figure S14) show that the peak currents quickly increase from cycle #1 to cycle #2 and stabilize in cycle #3 with two pairs of redox peaks. In contrast, the stabilized CV of the Na-V₂O₅ NR/rGO cathode does not have clear redox peaks (Figure S15). More charge-discharge curves and CVs of Zn-V₂O₅ NR/rGO and (Mn + Zn)-V₂O₅ NR/rGO are presented in Figure S16. As the scan rate is increased from 0.50 to 2.0 mV s⁻¹, the peak separation increases to more than 350 mV, further indicating the slow kinetics of Zn²⁺ ion insertion/extraction.

One of the topics of interest in AZIBs is whether water or H⁺ ions are involved in the electrochemical reactions. CV studies in 0.010 M H_2SO_4 at pH = 1.70 (Figure S17) show that hydrogen evolution reaction is not involved in the AZIB conditions, but H+ intercalation into the V2O5 NR cathode does occur. The ex situ XRD measurements (Figure S18) show that it forms a new Zn₄SO₄(OH)₆·4H₂O phase after the Zn-V₂O₅ NR/rGO and (Mn + Zn)-V₂O₅ NR/rGO cathodes are discharged and it disappears after being completely charged. H⁺ ions may intercalate into the V₂O₅ NRs during discharge, leading to an increase in the local pH value and formation of Zn₄SO₄(OH)₆·4H₂O crystals (possibly at the exterior surface of V₂O₅ NRs). Since it is reversible, H⁺ participation is beneficial and boosts the specific capacity, exceeding the theoretical values of 294 mAh g^{-1} for V_2O_5 , as shown in Figure 5a. Considering the much lower H⁺ concentration ($\sim 10^{-7}$ M) than that of Zn2+ (2.0 M) in the AZIB electrolyte, the contribution of H+ ions may be relatively small. It is worth investigating to quantify the $H^{\scriptscriptstyle +}$ participation in future studies.

The enhanced performance of the AZIBs in this study is attributed to improved Zn^{2+} ion intercalation into the divalent

ion-expanded V_2O_5 NR cathode. This is supported by the measurements with a galvanostatic intermittent titration technique (GITT). Figures S19 and S20 illustrate the GITT results for the AZIBs with the cathode made of (a) V_2O_5 NR, (b) Na- V_2O_5 NR/rGO, (c) Zn- V_2O_5 NR/rGO, and (d) (Mn + Zn)- V_2O_5 NR/rGO. The amplitudes of the voltage modulation in the GITT pulses clearly exhibit a descending trend among these materials, which qualitatively indicates the increase in the diffusion coefficient of Zn^{2+} ions (D_{Zn}^{2+}) in them. Table S4 shows that the estimated D_{Zn}^{2+} value follows the order: divalent ion expanded > monovalent cation expanded > pristine V_2O_5 NRs.

CONCLUSIONS

In summary, we report the scalable facile synthesis of hybrid materials M-V₂O₅ NR/rGO as high-performance cathodes for future sustainable AZIBs. Divalent metal ions M²⁺ (including Zn²⁺ and Mn²⁺) are used to effectively neutralize the negative charges on the surface of microwave-exfoliated V₂O₅ NRs and GO nanosheets to form a strongly bound V₂O₅ NR/GO assembly by coprecipitation. A thermal annealing process in the nitrogen atmosphere converts the GO to rGO nanosheets, which serve as the stable nanostructured template and highly conductive electron pathway. At the meantime, the singlecrystalline V₂O₅ NRs are converted into disordered V₂O₅ materials due to divalent metal cation insertion. Thus-formed M-V₂O₅ NR/rGO hybrid materials have shown improved electron transport and enhanced diffusion for Zn²⁺ ions during the charge-discharge processes. The Zn-V₂O₅ NR/rGO hybrid, with the elemental formula of the active host material as $Zn_{0.42}V_2O_{7.54}$, presents a very high reversible specific capacity of \sim 395 mAh g⁻¹ at 0.50 A g⁻¹ but poor stability. By mixing a fraction of Mn²⁺ with the Zn²⁺ ions during the coprecipitation process, a binary divalent metal cationmediated hybrid (Mn + Zn)-V₂O₅ NR/rGO is obtained, in which the active host material has an atomic formula of Zn_{0.12}Mn_{0.14}V₂O_{7.16}. The long-cycling stability and rate performance are substantially improved, while a relatively high specific capacity of \sim 291 mAh g⁻¹ at 0.5 A g⁻¹ is retained. The stronger binding of Mn^{n+} ions (n = 2, 3, and 4) with the V₂O₅ host makes them as more stable pillars to support the expanded V₂O₅ layers and enables the stronger attachment of the V₂O₅ host to rGO templates. This strategy is effective to balance the need for high specific capacity and good longcycling stability, which is comparable to the state-of-the-art work by other synthesis methods summarized in Table S5.

ASSOCIATED CONTENT

Solution Supporting Information

The Supporting Information is available free of charge at https://pubs.acs.org/doi/10.1021/acssuschemeng.2c07629.

Additional details of experimental procedures, optical images of the samples at various stages of synthesis, zeta potential values of rGO and $\rm V_2O_5$ NRs, TEM images of commercial $\rm V_2O_5$ powder and $\rm V_2O_5$ NRs, crystal structure of $\alpha\text{-}\rm V_2O_5$, more SAED pattern of $\rm V_2O_5$ NRs and analysis, control XRD of the sample holder, XPS spectra, analyses and table summary, TGA curves, analysis description and table summary, Zn²+ ion storage tests of various control samples (including Na-V₂O₅ NR/rGO cathode), charge—discharge curves at different cycles during initial long cycling, CV curves of initial

cycles, comparison of the stabilized M- $\rm V_2O_5$ NR/rGO cathodes, extensive charge—discharge curves and CV curves at different rates, CV assessment of hydrogen evolution and intercalation in AZIBs, ex situ XRD characterization, GITT measurements, and table for comparison with the literature (PDF)

AUTHOR INFORMATION

Corresponding Author

Jun Li – Department of Chemistry, Kansas State University, Manhattan, Kansas 66506, United States; oorcid.org/ 0000-0002-3689-8946; Email: junli@ksu.edu

Authors

Kamalambika Muthukumar – Department of Chemistry, Kansas State University, Manhattan, Kansas 66506, United States

Sabari Rajendran – Department of Chemistry, Kansas State University, Manhattan, Kansas 66506, United States

Archana Sekar — Department of Chemistry, Kansas State University, Manhattan, Kansas 66506, United States;
orcid.org/0000-0003-2171-7900

Ya Chen – School of Metallurgy and Environment, Central South University, Changsha, Hunan 410083, China

Complete contact information is available at: https://pubs.acs.org/10.1021/acssuschemeng.2c07629

Notes

The authors declare no competing financial interest.

ACKNOWLEDGMENTS

This work is supported by the National Science Foundation under grant DMR-1707585 and partially under CBET-1703263 and CBET-2054754. We thank Dr. Dan Boyle at Kansas State University's microscopy facility for help in TEM/SAED measurements and Prof. Christer Aakeroy at Kansas State University for support in TGA measurements. The XPS characterization was performed in the Nebraska Nanoscale Facility supported by the National Science Foundation under Award ECCS: 2025298 and the Nebraska Research Initiative.

■ REFERENCES

- (1) Service, R. F. Zinc Aims to Beat Lithium Batteries at Storing Energy. *Science* **2021**, *372*, 890–891.
- (2) Ming, J.; Guo, J.; Xia, C.; Wang, W.; Alshareef, H. N. Zinc-ion batteries: Materials, mechanisms, and applications. *Mater. Sci. Eng., R* **2019**, *135*, 58–84.
- (3) Jia, X.; Liu, C.; Neale, Z. G.; Yang, J.; Cao, G. Active Materials for Aqueous Zinc Ion Batteries: Synthesis, Crystal Structure, Morphology, and Electrochemistry. *Chem. Rev.* **2020**, *120*, *7795*–7866.
- (4) Konarov, A.; Voronina, N.; Jo, J. H.; Bakenov, Z.; Sun, Y.-K.; Myung, S.-T. Present and Future Perspective on Electrode Materials for Rechargeable Zinc-Ion Batteries. *ACS Energy Lett.* **2018**, *3*, 2620–2640.
- (5) Liang, X.; Yan, L.; Li, W.; Bai, Y.; Zhu, C.; Qiang, Y.; Xiong, B.; Xiang, B.; Zou, X. Flexible high-energy and stable rechargeable vanadium-zinc battery based on oxygen defect modulated V₂O₅ cathode. *Nano Energy* **2021**, *87*, No. 106164.
- (6) Bock, C. W.; Katz, A. K.; Glusker, J. P. Hydration of Zinc Ions: A Comparison with Magnesium and Beryllium Ions. *J. Am. Chem. Soc.* **1995**, *117*, 3754–3765.

- (7) Zhou, J.; Shan, L.; Wu, Z.; Guo, X.; Fang, G.; Liang, S. Investigation of V_2O_5 as a low-cost rechargeable aqueous zinc ion battery cathode. *Chem. Commun.* **2018**, *54*, 4457–4460.
- (8) Chen, T.; Zhu, X.; Chen, X.; Zhang, Q.; Li, Y.; Peng, W.; Zhang, F.; Fan, X. VS₂ nanosheets vertically grown on graphene as high-performance cathodes for aqueous zinc-ion batteries. *J. Power Sources* **2020**, 477, No. 228652.
- (9) Alfaruqi, M. H.; Islam, S.; Gim, J.; Song, J.; Kim, S.; Pham, D. T.; Jo, J.; Xiu, Z.; Mathew, V.; Kim, J. A high surface area tunnel-type α -MnO₂ nanorod cathode by a simple solvent-free synthesis for rechargeable aqueous zinc-ion batteries. *Chem. Phys. Lett.* **2016**, 650, 64–68.
- (10) Li, H.; Yang, Q.; Mo, F.; Liang, G.; Liu, Z.; Tang, Z.; Ma, L.; Liu, J.; Shi, Z.; Zhi, C. MoS_2 nanosheets with expanded interlayer spacing for rechargeable aqueous Zn-ion batteries. *Energy Storage Mater.* **2019**, 19, 94–101.
- (11) Wang, B.; Han, Y.; Wang, X.; Bahlawane, N.; Pan, H.; Yan, M.; Jiang, Y. Prussian blue analogs for rechargeable batteries. *Iscience* **2018**, *3*, 110–133.
- (12) Cheah, Y. L.; Aravindan, V.; Madhavi, S. Improved Elevated Temperature Performance of Al-Intercalated V_2O_5 Electrospun Nanofibers for Lithium-Ion Batteries. *ACS Appl. Mater. Interfaces* **2012**, *4*, 3270–3277.
- (13) Su, D. W.; Dou, S. X.; Wang, G. X. Hierarchical orthorhombic V_2O_5 hollow nanospheres as high performance cathode materials for sodium-ion batteries. *J. Mater. Chem. A* **2014**, *2*, 11185–11194.
- (14) Liu, M.; Su, B.; Tang, Y.; Jiang, X.; Yu, A. Recent Advances in Nanostructured Vanadium Oxides and Composites for Energy Conversion. *Adv. Energy Mater.* **2017**, *7*, 1700885.
- (15) Schoiswohl, J.; Surnev, S.; Netzer, F. P.; Kresse, G. Vanadium oxide nanostructures: from zero- to three-dimensional. *J. Phys.: Condens. Matter* **2006**, *18*, R1–R14.
- (16) Wang, X.; Li, Y.; Wang, S.; Zhou, F.; Das, P.; Sun, C.; Zheng, S.; Wu, Z.-S. 2D Amorphous V₂O₅/Graphene Heterostructures for High-Safety Aqueous Zn-Ion Batteries with Unprecedented Capacity and Ultrahigh Rate Capability. *Adv. Energy Mater.* **2020**, *10*, 2000081.
- (17) NIST Atomic Spectra Database. http://physlab2.nist.gov/cgi-bin/AtData/main_asd (accessed May 16).
- (18) Kundu, D.; Adams, B. D.; Duffort, V.; Vajargah, S. H.; Nazar, L. F. A high-capacity and long-life aqueous rechargeable zinc battery using a metal oxide intercalation cathode. *Nat. Energy* **2016**, *1*, 16119.
- (19) He, P.; Zhang, G.; Liao, X.; Yan, M.; Xu, X.; An, Q.; Liu, J.; Mai, L. Sodium Ion Stabilized Vanadium Oxide Nanowire Cathode for High-Performance Zinc-Ion Batteries. *Adv. Energy Mater.* **2018**, 8, 1702463.
- (20) Xia, C.; Guo, J.; Li, P.; Zhang, X.; Alshareef, H. N. Highly Stable Aqueous Zinc-Ion Storage Using a Layered Calcium Vanadium Oxide Bronze Cathode. *Angew. Chem., Int. Ed.* **2018**, *57*, 3943–3948.
- (21) Islam, S.; Alfaruqi, M. H.; Putro, D. Y.; Soundharrajan, V.; Sambandam, B.; Jo, J.; Park, S.; Lee, S.; Mathew, V.; Kim, J. K^+ intercalated V_2O_5 nanorods with exposed facets as advanced cathodes for high energy and high rate zinc-ion batteries. *J. Mater. Chem. A* **2019**, 7, 20335–20347.
- (22) Levi, E.; Gofer, Y.; Aurbach, D. On the Way to Rechargeable Mg Batteries: The Challenge of New Cathode Materials. *Chem. Mater.* **2010**, *22*, 860–868.
- (23) De Juan-Corpuz, L. M.; Corpuz, R. D.; Somwangthanaroj, A.; Nguyen, M. T.; Yonezawa, T.; Ma, J.; Kheawhom, S. Binder-Free Centimeter-Long V_2O_5 Nanofibers on Carbon Cloth as Cathode Material for Zinc-Ion Batteries. *Energies* **2020**, *13*, 31.
- (24) Chen, Y.; Muthukumar, K.; Leban, L.; Li, J. Microwave-assisted high-yield exfoliation of vanadium pentoxide nanoribbons for supercapacitor applications. *Electrochim. Acta* **2020**, 330, No. 135200.
- (25) De Jesus, J. C.; González, I.; Quevedo, A.; Puerta, T. Thermal decomposition of nickel acetate tetrahydrate: an integrated study by TGA, QMS and XPS techniques. *J. Mol. Catal. A: Chem.* **2005**, 228, 283–291.
- (26) Sun, J.; Liu, Y.; Jiang, H.; Dong, X.; Hu, T.; Meng, C.; Zhang, Y. Mn²⁺ as the "spearhead" preventing the trap of Zn²⁺ in layered

- Mn²⁺ inserted hydrated vanadium pentoxide enables high rate capacity. *J. Colloid Interface Sci.* **2021**, *602*, 14–22.
- (27) Liu, C.; Neale, Z.; Zheng, J.; Jia, X.; Huang, J.; Yan, M.; Tian, M.; Wang, M.; Yang, J.; Cao, G. Expanded hydrated vanadate for high-performance aqueous zinc-ion batteries. *Energy Environ. Sci.* **2019**, *12*, 2273–2285.
- (28) Geng, H.; Cheng, M.; Wang, B.; Yang, Y.; Zhang, Y.; Li, C. C. Electronic Structure Regulation of Layered Vanadium Oxide via Interlayer Doping Strategy toward Superior High-Rate and Low-Temperature Zinc-Ion Batteries. *Adv. Funct. Mater.* **2020**, 30, 1907684.
- (29) Feng, Z.; Zhang, Y.; Sun, J.; Liu, Y.; Jiang, H.; Cui, M.; Hu, T.; Meng, C. Dual ions enable vanadium oxide hydration with superior Zn2+ storage for aqueous zinc-ion batteries. *Chem. Eng. J.* **2022**, 433, No. 133795.
- (30) Ng, S. H.; Chew, S. Y.; Wang, J.; Wexler, D.; Tournayre, Y.; Konstantinov, K.; Liu, H. K. Synthesis and electrochemical properties of V₂O₅ nanostructures prepared via a precipitation process for lithium-ion battery cathodes. *J. Power Sources* **2007**, *174*, 1032–1035.
- (31) Lee, H.; Kumbhar, V. S.; Lee, J.; Choi, Y.; Lee, K. Highly reversible crystal transformation of anodized porous V_2O_5 nanostructures for wide potential window high-performance supercapacitors. *Electrochim. Acta* **2020**, 334, No. 135618.
- (32) Tepavcevic, S.; Xiong, H.; Stamenkovic, V. R.; Zuo, X.; Balasubramanian, M.; Prakapenka, V. B.; Johnson, C. S.; Rajh, T. Nanostructured Bilayered Vanadium Oxide Electrodes for Rechargeable Sodium-Ion Batteries. *ACS Nano* **2012**, *6*, 530–538.
- (33) Liu, F.; Chen, Z.; Fang, G.; Wang, Z.; Cai, Y.; Tang, B.; Zhou, J.; Liang, S. V₂O₅ Nanospheres with Mixed Vanadium Valences as High Electrochemically Active Aqueous Zinc-Ion Battery Cathode. *Nano-Micro Lett.* **2019**, *11*, 25.
- (34) Qin, X.; Wang, X.; Sun, J.; Lu, Q.; Omar, A.; Mikhailova, D. Polypyrrole Wrapped V₂O₅ Nanowires Composite for Advanced Aqueous Zinc-Ion Batteries. *Front. Energy Res.* **2020**, *8*, 199.
- (35) Chen, D.; Yi, R.; Chen, S.; Xu, T.; Gordin, M. L.; Lv, D.; Wang, D. Solvothermal synthesis of V_2O_5/g raphene nanocomposites for high performance lithium ion batteries. *Mater. Sci. Eng., B* **2014**, *185*, 7–12.
- (36) Li, Y.; Huang, Z.; Kalambate, P. K.; Zhong, Y.; Huang, Z.; Xie, M.; Shen, Y.; Huang, Y. V_2O_5 nanopaper as a cathode material with high capacity and long cycle life for rechargeable aqueous zinc-ion battery. *Nano Energy* **2019**, *60*, 752–759.
- (37) Thiagarajan, S.; Thaiyan, M.; Ganesan, R. Physical vapor deposited highly oriented V_2O_5 thin films for electrocatalytic oxidation of hydrazine. *RSC Adv.* **2016**, *6*, 82581–82590.
- (38) Rehnlund, D.; Valvo, M.; Edström, K.; Nyholm, L. Electrodeposition of Vanadium Oxide/Manganese Oxide Hybrid Thin Films on Nanostructured Aluminum Substrates. *J. Electrochem. Soc.* **2014**, *161*, D515–D521.
- (39) Zhu, Y.-J.; Chen, F. Microwave-Assisted Preparation of Inorganic Nanostructures in Liquid Phase. *Chem. Rev.* **2014**, *114*, 6462–6555.
- (40) Zhu, Y.-H.; Zhang, Q.; Yang, X.; Zhao, E.-Y.; Sun, T.; Zhang, X.-B.; Wang, S.; Yu, X.-Q.; Yan, J.-M.; Jiang, Q. Reconstructed Orthorhombic V_2O_5 Polyhedra for Fast Ion Diffusion in K-Ion Batteries. *Chem* **2019**, *5*, 168–179.
- (41) Bera, B.; Sekhar Das, P.; Bhattacharya, M.; Ghosh, S.; Mukhopadhyay, A. K.; Dey, A. Nanoscale contact resistance of V_2O_5 xerogel films developed by nanostructured powder. *J. Phys. D: Appl. Phys.* **2016**, 49, No. 085303.
- (42) Ye, G.; Gong, Y.; Keyshar, K.; Husain, E. A. M.; Brunetto, G.; Yang, S.; Vajtai, R.; Ajayan, P. M. 3D Reduced Graphene Oxide Coated V_2O_5 Nanoribbon Scaffolds for High-Capacity Supercapacitor Electrodes. *Part. Part. Syst. Charact.* **2015**, 32, 817–821.
- (43) Castriota, M.; Cazzanelli, E.; Fasanella, A.; Teeters, D. Electrical conductivity and Raman characterization of V_2O_5 grown by sol–gel technique inside nanoscale pores. *Thin Solid Films* **2014**, 553, 127–131.
- (44) Weimer, M. S.; Kim, I. S.; Guo, P.; Schaller, R. D.; Martinson, A. B. F.; Hock, A. S. Oxidation State Discrimination in the Atomic

- Layer Deposition of Vanadium Oxides. Chem. Mater. 2017, 29, 6238–6244.
- (45) Cui, P.; Lee, J.; Hwang, E.; Lee, H. One-pot reduction of graphene oxide at subzero temperatures. *Chem. Commun.* **2011**, 47, 12370–12372.
- (46) Avansi, W., Jr.; Ribeiro, C.; Leite, E. R.; Mastelaro, V. R. Vanadium Pentoxide Nanostructures: An Effective Control of Morphology and Crystal Structure in Hydrothermal Conditions. *Cryst. Growth Des.* **2009**, *9*, 3626–3631.
- (47) Zhu, J.; Shen, H.; Shi, X.; Yang, F.; Hu, X.; Zhou, W.; Yang, H.; Gu, M. Revealing the Chemical and Structural Evolution of $\rm V_2O_5$ Nanoribbons in Lithium-Ion Batteries Using in Situ Transmission Electron Microscopy. *Anal. Chem.* **2019**, *91*, 11055–11062.
- (48) He, P.; Chen, S. Cathode strategies to improve the performance of zinc-ion batteries. *Electrochem. Sci. Adv.* **2022**, *2*, No. e2100090.
- (49) He, P.; Yan, M.; Liao, X.; Luo, Y.; Mai, L.; Nan, C.-W. Reversible V³⁺/V⁵⁺ double redox in lithium vanadium oxide cathode for zinc storage. *Energy Storage Mater.* **2020**, *29*, 113–120.
- (50) Ridley, P.; Gallano, C.; Andris, R.; Shuck, C. E.; Gogotsi, Y.; Pomerantseva, E. MXene-Derived Bilayered Vanadium Oxides with Enhanced Stability in Li-Ion Batteries. *ACS Appl. Energy Mater.* **2020**, 3, 10892–10901.
- (51) Yang, Y.; Tang, Y.; Liang, S.; Wu, Z.; Fang, G.; Cao, X.; Wang, C.; Lin, T.; Pan, A.; Zhou, J. Transition metal ion-preintercalated $\rm V_2O_5$ as high-performance aqueous zinc-ion battery cathode with broad temperature adaptability. Nano Energy 2019, 61, 617–625.
- (52) Zhao, X.; Yan, Y.; Mao, L.; Fu, M.; Zhao, H.; Sun, L.; Xiao, Y.; Dong, G. A relationship between the V^{4+}/V^{5+} ratio and the surface dispersion, surface acidity, and redox performance of V_2O_5 – WO_3 / TiO_2 SCR catalysts. *RSC Adv.* **2018**, *8*, 31081–31093.
- (53) Deng, X.; Xu, Y.; An, Q.; Xiong, F.; Tan, S.; Wu, L.; Mai, L. Manganese ion pre-intercalated hydrated vanadium oxide as a high-performance cathode for magnesium ion batteries. *J. Mater. Chem. A* **2019**, *7*, 10644–10650.

□ Recommended by ACS

An Advanced Alkaline Al-Air Fuel Cell Using l-Ascorbic Acid Interface Layer upon Al Anode via Gradient Anticorrosion

Manhui Wei, Pucheng Pei, et al.

FEBRUARY 22, 2023

ACS SUSTAINABLE CHEMISTRY & ENGINEERING

READ 🗹

In Situ Investigation on the Morphology and Formation Kinetics of a CO_2/N_2 Mixed Hydrate Film

Yu-Jie Zhu, Guang-Jin Chen, et al.

MARCH 10, 2023

ACS SUSTAINABLE CHEMISTRY & ENGINEERING

READ 🗹

Concurrently Engineered Lewis Acid Sites and Coordination Sphere Vacancies in CoFe Prussian Blue Analogues for Boosted Bifunctional Oxygen Electrocatalysis

Priya Jain, Pravin Popinand Ingole, et al.

MARCH 10, 2023

ACS APPLIED ENERGY MATERIALS

READ **C**

Mo-Pre-Intercalated MnO₂ Cathode with Highly Stable Layered Structure and Expanded Interlayer Spacing for Aqueous Zn-Ion Batteries

Zhen Wang, Ping Li, et al.

DECEMBER 29, 2022

ACS APPLIED MATERIALS & INTERFACES

READ 🗹

Get More Suggestions >